Simulation and Assessment of Readout Electronics for Scintillation Light in Liquid Xenon for Nuclear Medical Imaging Systems

EL Mehdi Rtimi[1,*], *Domique* Thers[2], and *Marc-André* Tétrault[1]

[1]Interdisciplinary Institute for Technological Innovation - 3iT, Université de Sherbrooke, Canada
[2]Subatech, IMT-Atlantique CNRS / IN2P3, Université de Nantes, France

Abstract. This paper presents the simulation and evaluation of a proposed cryogenic front-end electronics (FEE) system designed to detect scintillation light generated in the XEMIS (Xenon Medical Imaging Systems) application. This nuclear medical imaging modality aims to reduce the injected activity in patients while enhancing spatial resolution by applying a three-gamma imaging technique and employing liquid xenon in time projection chamber (LXe-TPC) as a detector.

This work aims to replace the current FEE, XSRETOT (XEMIS Scintillation Readout for Extraction of Time Over Threshold), in the XEMIS application. The new FEE is designed to facilitate scalability for future iterations, including a full-body version of XEMIS. This system, intended for clinical applications, spans a 2-meter axial length and aims to achieve high detection sensitivity, low power consumption, and cost-effectiveness.

The proposed methodology entailed simulating the replacement of the 30×30 mm² photomultiplier tube with a 4×4 array of VUV-MPPCs (Vacuum Ultraviolet - Multi-Pixel Photon Counters), each measuring 6×6 mm². We assessed three types of FEE for their detection efficiency. Based on the results, we identified the design with a commercial cryogenic transimpedance amplifier and a sigma-delta modulator based on the SiGe HBT technology as the most suitable. The optimized FEE will then be developed and tested at the operating temperature of the LXe-TPC.

1 Introduction

Since the 1950s, functional nuclear medical imaging has attracted growing interest within the scientific community. In the early 1970s, the introduction of SPECT (Single Photon Emission Computed Tomography) and PET (Positron Emission Tomography) marked a breakthrough in the diagnosis and investigation of molecular imaging [1].

In the case of PET imaging, these techniques rely on the administration of a radioactive tracer that interacts with cellular components of the body. As shown in the Figure 1, each interaction results in a pair of 511 keV gamma photons emitted back-to-back, resulting from the annihilation of a positron with an electron. The information related to the timing, energy,

*e-mail: rtie2001@usherbrooke.ca

and position of these events is then captured and recorded by pixelized radiation detectors, enabling the reconstruction of three-dimensional medical images. The design of these imaging systems must balance two fundamental requirements: minimizing patient radiation exposure while ensuring high detection efficiency[2] by maximizing the sensitivity, which is essential for accurate, high-resolution imaging. This trade-off remains a key focus of current research.

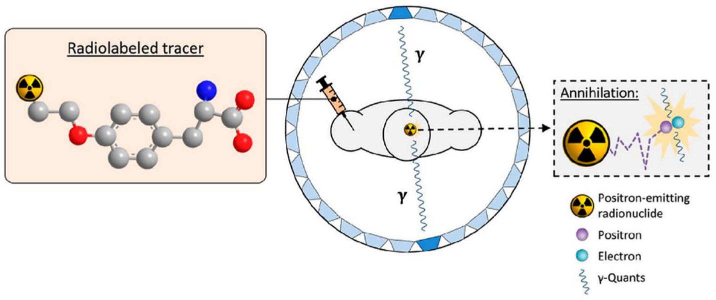

Figure 1: Principles of Positron Emission Tomography imaging, taken from [3].

To address these challenges, the development of these systems is progressing on multiple fronts. On one hand, new imaging modalities are emerging, such as Time-of-Flight PET [4], three-gamma imaging [5], and hybrid approaches [6]. On the other hand, considerable efforts are being made to optimize detection technologies, particularly photodetectors and the associated readout and acquisition electronics. Finally, the design of a whole-body detector with a 2-meter field of view can significantly enhance sensitivity by a factor of up to 40 or offer other advantages, such as reduced scan time or lower injected activity [7].

In line with these advancements, XEMIS has emerged as a promising approach for full-body imaging with low injected activity. It leverages the 3-gamma imaging modality by using (β^+, γ) emitters, such as scandium-44 [5], which emit a gamma ray nearly simultaneously with the β^+ decay seen in PET. The third gamma thus provides additional spatial and background noise reduction information.

Unlike other experiments such as PETALO (Positron Emission TOF Apparatus with Liquid xenOn) [8], which use liquid xenon as a scintillation medium to enhance the performance of ToF-PET systems, XEMIS employs liquid xenon in a time projection chamber (LXe-TPC) configuration, operated at 165K.

This work is a first look to scale up the readout electronics from the R&D prototype (XEMIS-1) onto a future full-body clinical model (XEMIS-3), while maintaining low noise, low power consumption, and enhanced sensitivity.

2 Detector Overview

2.1 XEMIS concept

The detector based on XEMIS technology uses liquid xenon in a Time Projection Chamber (LXe-TPC) mode, maintained at a temperature of 165K. As shown in Figure 2, When a gamma ray enters the LXe-TPC, two nearly simultaneous interactions occur: scintillation, which generates photons in Vacuum Ultraviolet (VUV) at 175 nm, and ionization, which releases charges[9].

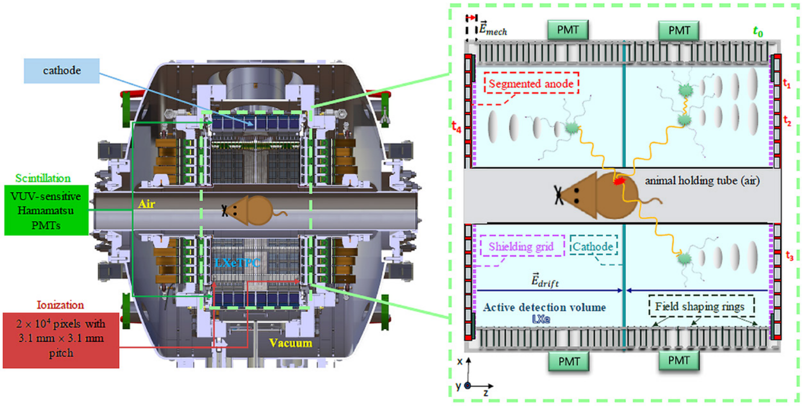

Figure 2: Schematic diagram of the principle of XEMIS2 in longitudinal view, taken from [9].

This detector integrates two complementary detection systems. The first, *XSRETOT* (XEMIS Scintillation Readout for Extraction of Time Over Threshold), detects VUV light by using a 30x30mm² photomultiplier tube (PMT), allowing the determination of the initial arrival time t_0 and the estimated number of photonelectrons N_{pes}. The second system, *XTRACT* (Xenon TPC Readout for extrAction of Charge and Time), collects the charges using the TPC's electric field by directing them toward the anode, measuring the collected charges and their arrival time t_1. The XTRACT system also determines the interaction position along the X and Y axes, while the longitudinal position Z is obtained using Equation 1:

$$Z = \frac{V_{\text{drift}}}{t_1 - t_0} \tag{1}$$

where V_{drift} represents the drift velocity for a given electrical field potential.

2.2 XSRETOT overview

Each 30 × 30 mm² PMT, immersed in liquid xenon, is read out by a single XSRETOT channel operating at ambient temperature. This XSRETOT, as presented in Figure 3, includes a wideband operational amplifier designed to invert and amplify the PMT's analog signal by a factor of 10 while ensuring gain stability [9].

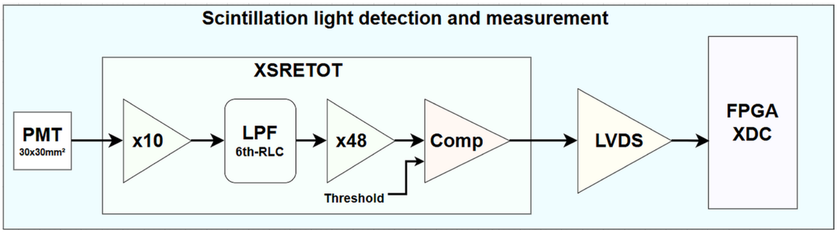

Figure 3: Schematic diagram of the XSRETOT used in XEMIS2.

A sixth-order RLC low-pass filter (LPF) acts as a passive shaper, integrating and shaping the PMT output signals. The shaped signal is then further amplified by an additional stage with a gain of 48. Finally, based on the Time over Threshold (ToT) technique, this method uses a comparator to detect when the amplified and integrated signal exceeds a predefined threshold, generating a logic pulse-shaped output. The width of these signals increases logarithmically with N_{pes}, while its leading edge indicates the arrival time t_0. This information from each channel is read out and digitized by the XDC (XEMIS Data Concentrator), which is based on a Field-Programmable Gate Array (FPGA) with a sampling frequency of about 200 MHz[9].

Currently, the results indicate that the XSRETOT electronics demonstrates effective performance in scintillation light measurement, meeting the requirements of the first preclinical stage of the XEMIS2 project, which involves 64 PMTs for small-animal imaging [9]. The XSRETOT can detect down to a few photons per PMT while operating with a $\pm 6V$ power supply and a power consumption of 550 mW per PMT. Meanwhile, the PMT itself functions with a 750V bias and an active area of 18×18 mm².

2.3 Outlook onto XEMIS-3

As an alternative to PMTs, MPPCs offer numerous advantages, including improved compactness [10], and better compatibility with cryogenic environments [11]. MPPCs are also sensitive to single photons, provide high internal gain, operate at low bias voltage ($< 60V$), low power consumption, and exhibit excellent time resolution. Furthermore, they are insensitive to magnetic fields and enable finer spatial resolution [12]. Altogether, they also provide a more practical solution to mechanical integration challenges, while enhancing scalability for large-scale detector systems, such as in the upcoming XEMIS-3 iteration.

Concurrently, scaling XEMIS to a full-body detector using either PMTs or MPPCs introduces several constraints [13], in particular mechanical limitations. By their smaller physical size and better sturdiness, MPPCs already have an advantage for the mecanical assembly of a large, full-body system. Additionally, direct scaling of the connectivity between the photosensors and their room-temperature electronics would require a prohibitive amount of cables, significantly increasing the size of the feedthrough connectors, and thus heat leaks. Therefore, a low power front-end readout electronics with digitization and data multiplexing should instead be placed close to the MPPC, while maintaining low noise and the ability to detect single photons. This appears feasible as some cryogenic analog front-end electronics have already demonstrated effectiveness with S13371-6050CQ-02 VUV-MPPC arrays, particularly in dark matter research projects [11], coupled with FPGAs compatible with low temperature cryogenic environments [14].

This study aims to first develop the analog cryogenic front-end electronics system to replace XRESTOT, for an eventual coupling with an FPGA for data multiplexing, embedded behind the MPPCs in the cryostat. This new system will incorporate a 4×4 VUV-MPPC array, with each channel measuring 6×6 mm², as a substitute for the current 30×30 mm² PMT.

3 6x6mm² Cryogenic Detector module

3.1 Introduction

This section, on the one hand, outlines the specifications of the 6×6mm² detection surface and introduces the three FEE selected for the simulation phase, based on scalability and detection requirements. On the other hand, it also discusses considerations for designing stable cryogenic FEE using commercial components based on silicon-germanium heterojunction bipolar transistor (SiGe HBT) technology, operating at temperatures as low as 165K.

3.2 Specifications

Replacing one channel of XSRETOT requires a 4×4 array of VUV-MPPC channels, each measuring 6×6 mm², based on the physical conditions of XEMIS2 [9]. Each scintillation event can produce up to 200 photoelectrons per PMT, following a Poisson distribution, which corresponds to approximately 12 p.e.s per individual 6×6 mm² VUV-MPPC (i.e., 200 p.e.s ÷ $16_{\text{VUV-MPPC}}$).

In addition to this substitution, the ability to detect single photons on each elementary detection area of 6×6 mm^2 is considered a critical requirement of the system. To meet this specification, the threshold must be set below the level corresponding to a single photoelectron. However, the XSRETOT threshold is currently configured at a level equivalent to 1p.e [9] which does not allow for such sensitivity.

Our approach begins with a simulation of three types of analog front-end electronics, as shown in Figure 4, to assess their performance in detecting p.e.s from a single 6×6 mm² VUV-MPPC and to evaluate the error estimation for each FEE.

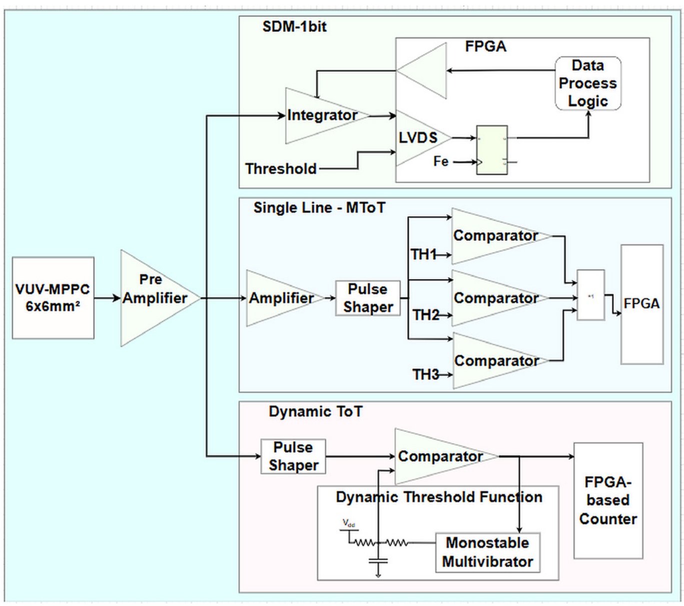

Figure 4: Schematic diagram of scintillation signals detection systems used in simulation.

1. Sigma Delta Modulation (SDM-1bit)[15] : This FEE is characterized by a simple mixed-signal design, utilizing an FPGA with GPIOs (General-Purpose Input/Output) configured in LVDS (Low-Voltage Differential Signaling) mode to act as comparators. This comparator is preceded by an integrator responsible for integrating the signal from the amplifier. The integrator is controlled by a discharge line driven by the FPGA, which accelerates the discharge process to optimize successive integrations of the scintillation signal.

   Furthermore, this approach enables the use of leading-edge and trailing-edge detectors to detect the signal pulse, relying on the time-over-threshold (ToT) technique implemented with an LVDS comparator. This enables the extraction of information on the number of N_{pes} and the arrival time t_0, provided that the signal exceeds the comparator threshold.

2. Single Line Multi-ToT[16]: Unlike the ToT approach, which relies on a single comparator, the multi-threshold technique utilizes three distinct levels (th_1, th_2, and th_3). The amplifier's output is fed into three comparators, generating three logic pulses of different widths (TOT_1, TOT_2, and TOT_3). These signals are then processed through a 3-input XOR logic gate, resulting in a single digital signal with six timestamps. These timestamps allow for the estimation of Npes by applying three different estimators at the XOR output: rectangular sum, trapezoidal sum and crossing point triangular sum.

   This FEE uses XOR-based multiplexing of the digital signals from the three thresholds, allowing them to be transmitted over a single line to the FPGA for data acquisition. This approach enhances the integrity of an FPGA-only data acquisition system by reducing the number of input channels required.

3. Dynamic ToT (DToT)[17]: Instead of relying on fixed or multiple predefined thresholds, the DToT technique introduces a dynamically varying threshold rather than a constant one. The shape of this dynamic threshold strongly depends on the characteristics of the analog input signal. As illustrated in Figure 4 , DToT is based on the Dynamic Threshold Function (DTF), which consists of a monostable multivibrator (MM) combined with an RC shaper circuit.
   When the analog input signal exceeds the initial threshold set by Vdd, the rising edge of the comparator output triggers the MM, generating a square pulse with a fixed duration and amplitude. This pulse is then added to the initial threshold, forming the new dynamic threshold. The amplitude and duration of the MM-generated pulse must be calibrated to match the pulse width corresponding to the maximum amplitude input signals. The comparator's output pulse is subsequently processed by an FPGA-based counter, which estimates the N_{pes} by sampling the comparator output.

3.3 Cryogenic Considerations

Several studies, particularly in the context of dark matter detection using liquid argon [18], [19], [20], have demonstrated that certain commercial FEE based on operational amplifiers using SiGe HBT technology exhibit superior stability at cryogenic temperatures compared to standard silicon bipolar junction transistors [21]. In parallel, other studies have characterized the performance of specific MPPCs under cryogenic conditions. The following subsections present the results of these characterizations, which can lead to the design of a stable 6×6mm² detector module operating at 165K.

Cryogenic effects on SiGe HBT FEE

The cryogenic effects reported in the literature, particularly those using the SiGe HBT LMH6629 [18] and LMH6624 operational amplifiers [20], indicate a reduction in total output noise. This improvement is primarily attributed to the decrease in both input voltage and current noise. For example, the LMH6624 exhibits an input voltage noise of $0.95\,\mathrm{nV}/\sqrt{\mathrm{Hz}}$ at 300 K, which decreases to approximately $0.53\,\mathrm{nV}/\sqrt{\mathrm{Hz}}$ at 77 K [20].

In addition, the gain–bandwidth product (GBP) of the LMH6629 increases with decreasing temperature, with a reported bandwidth rise of 189kHz/°C for a fixed gain [18]. Conversely, for the LMH6624, GBP variation with supply voltage is minor at room temperature but can double at 77K [20].

Moreover, since jitter depends on the ratio of electronic noise to the signal's slew rate at threshold crossing, reducing output noise lowers jitter. Under these conditions, jitter becomes mainly limited by the slew rate, with a reported decrease of approximately 0.05ns/°C [18].

Cryogenic effects on MPPC

First, the gain is directly dependent on the overvoltage $V_{\mathrm{ov}} = V_{\mathrm{bias}} - V_{\mathrm{br}}$, where the breakdown voltage V_{br} is temperature-dependent[22]. This effect can be compensated during calibration by adjusting the bias voltage to maintain the desired gain.

Second, the DCR strongly depends on temperature and overvoltage. At 165 K, it drops to 0.1 Hz/mm^2 [25], compared to 4 MHz/mm^2 at 300K, a reduction of nearly seven orders of magnitude. This very low DCR represents a negligible noise contribution under experimental and operating conditions, and does not affect the photon counting efficiency, even at low numbers of Npes. Rather, lower temperatures improves the MPPCs effectiveness in this regard.

Finally, low operating temperatures increase the avalanche quenching time, or decay time ($t_d = C_d \cdot R_d$) of the MPPC output signal, mainly due to a rise in the quenching resistor R_d [22, 23]. This affects the Npes–ToT linearity but can be mitigated by adjusting the threshold level during the calibration process. The rise time also increases slightly, as reported in [18], from 6 ns to 8 ns at 77 K, which can be compensated by tuning the bandwidth of the cryogenic FEE.

These cryogenic prior studies demonstrate the feasibility of designing a stable cryogenic detector combining an S13371-6050CQ-02 VUV-MPPC with FEE based on commercial SiGe HBT amplifier technology. They also highlight that cryogenic temperature-induced variations are either negligible or even beneficial. Moreover, such variations can often be compensated through calibration. Building on these considerations, the same design approach can be confidently extended to liquid xenon temperatures at 165K, as the underlying effects of temperature variations remain consistent across this range.

4 Simulation process

As described earlier in Section 2.1, the XSRETOT FEE serves two primary functions:

(a) Estimate the N_{pes}.

(b) Determine the arrival time of detected photons t_0.

To assess the effectiveness of the proposed approach, the simulation primarily focused on identifying the most suitable FEE for photon counting, with particular attention to pile-up effects and single-photon sensitivity, based on the estimation of $\mathrm{N}_{\mathrm{p.e.s}}$ and the evaluation of its associated error.

Additionally, given the cryogenic effects on the MPPC and FEE discussed in Section 3.3, these were excluded from the model, as they can be compensated during calibration and through appropriate architectural trade-offs. Including them in the simulation would have introduced unnecessary complexity; it is therefore more appropriate to characterize these effects experimentally once the final FEE has been selected.

Algorithm 1 illustrates the simulation process, implemented in Python, for a detection surface of 6×6 mm² over 50,000 samples.

Algorithm 1 High-Level Pseudocode of the Simulation Process

Initialization:
$T_{\text{Observation}} = 250$ ns, $T_{\text{Decay}} = 36$ ns, $T_{\text{Clk}} = 5$ ns, $N^{\text{Max}}_{\text{pes}} = 10$, $N = 50{,}000$, $ToT_{\text{1P.E.}} = 14$ ns, Threshold = 30 mV, $TiA_{\text{Gain}} = 3\text{K}$, $VUV - MPPC_{\text{Gain}} = 2.5 \times 10^6$
$i \leftarrow 1$
while $i \leq N$ **do**
  Generate Scintillation Event:
  $N_{\text{event}} \leftarrow \text{int}(T_{\text{Observation}}/T_{\text{Decay}})$
  $t_{\text{gen}}[1 : N_{\text{event}}] \sim \text{Exp}(1000)$
  $N^{\text{generated}}_{\text{pes}}[1 : N_{\text{event}}] \sim \text{Poisson}(5)$
  VUV-MPPC Signal Generation:
  for $j = 1$ to N_{event} **do**
    $V_{\text{VUV-MPPC}}[j] \leftarrow \text{VUV-MPPC}_{\text{gain}} \cdot \exp\left(-\frac{t_{\text{gen}}[j]-t}{T_{\text{recovery}}}\right)$
  end for
  Preamplifier Stage:
  for $j = 1$ to N_{event} **do**
    $V_{\text{preamp}}[j] \leftarrow \text{Preamplifier}_{\text{gain}} \cdot V_{\text{VUV-MPPC}}[j]$
  end for
  Front-End Electronics Processing:
  for $j = 1$ to N_{event} **do**
    $ToT_{\text{FEE}}[j] \leftarrow \text{FEE}(V_{\text{preamp}}[j] \cdot T_{\text{Clk}})$
    $N^{\text{estimated}}_{\text{pes}}[j] \leftarrow \sum_{j=1}^{N_{\text{event}}} \frac{ToT_{\text{FEE}}[j]}{ToT_{\text{1P.E.}}}$
  end for
  FEE Error Estimation:
  $\text{Error}[i] \leftarrow N^{\text{estimated}}_{\text{pes}}[i] - N^{\text{generated}}_{\text{pes}}[i]$
  $i \leftarrow i + 1$
end while
Histogram and Analysis of FEE Output

For each sample, the $N^{\text{generated}}_{\text{pes}}$ and their corresponding emission times t_{gen} are randomly generated to simulate scintillation events, which serve as the input to the simulation.

Figure 5a shows the distribution of simulated $N^{\text{generated}}_{\text{pes}}$ over 50,000 samples, following a Poisson distribution with a mean of 5 p.e.s per 6×6 mm² channel.

Additionally, the emission time of each p.e.s is randomly generated based on the VUV scintillation decay time in liquid xenon, within the defined observation window. This is illustrated in Figure 5b, which displays the expected exponential decay behavior. It can be observed that 80% of the p.e.s are emitted within the first 50 ns.

The simulation is carried out in several stages; for each sample, the $N^{\text{generated}}_{\text{pes}}$ and their corresponding emission time t_{gen} are converted into low-amplitude analog signals at the output of the VUV-MPPC, whose response is modeled by an analytical exponential function [28], [29]. These signals are then preamplified with a gain of 3k, simulating the response of a transimpedance (TiA) amplifier. Subsequently, they are injected into three FEE circuits to assess their ability to estimate $N^{\text{estimated}}_{\text{pes}}$ at the output, based on the

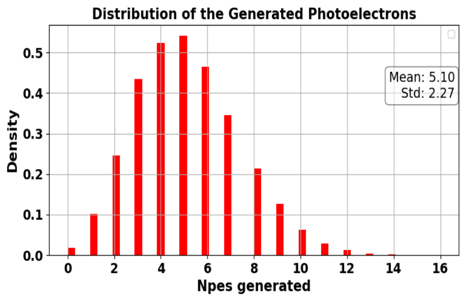

(a) The distribution of the generated number of photoelectrons.

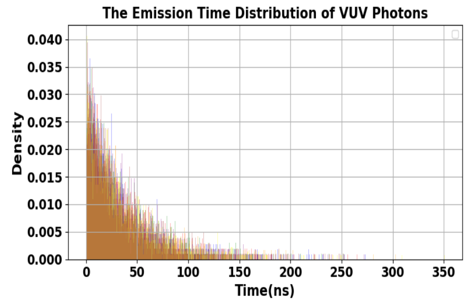

(b) The distribution of the VUV emission time in the LXe-TPC.

Figure 5: Distributions used to model the generated photoelectrons and the VUV emission time in the LXe-TPC.

specific characteristics of each FEE, as shown in Figure 4, and the XEMIS 5 ns sampling clock. Finally, the error between the $N_{\text{pes}}^{\text{estimated}}$ and $N_{\text{pes}}^{\text{generated}}$ is computed for each event. This process is repeated 50,000 times for each FEE type, yielding error histograms that reflect their performance in $N_{\text{pes}}^{\text{estimated}}$, including under pile-up conditions.

5 Results

5.1 Sigma delta modulator (SDM-1Bit)

The Time Over Threshold (ToT) output of the SDM-1Bit FEE, as shown in Figure 6, follows a Poisson-like distribution over 50,000 samples, with a mean value of 66.63 ns. This is nearly consistent with the input mean presented in Figure 5a, considering that the ToT of a single photoelectron corresponds to 14 ns. We can clearly distinguish individual photoelectrons, even in the presence of pile-up.

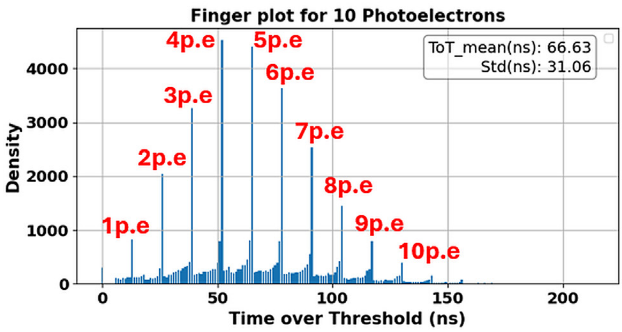

Figure 6: Finger plot diagram of the Time Over Threshold.

However, when examining the distribution of $N_{\text{pes}}^{\text{estimated}}$ over 50,000 samples, as shown in Figure 7, certain discrepancies become apparent when compared to the distribution of the $N_{\text{pes}}^{\text{generated}}$. For instance, both overestimation and underestimation can be observed depending on estimation parameters such as the ToT of a single photoelectron and the integration constants.

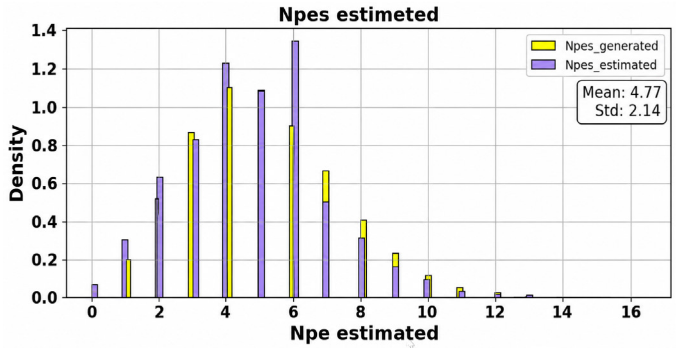

Figure 7: The distribution of Npes generated vs Npes estimated.

As part of the modeling process, Sobol sensitivity analysis[30] was employed to identify the optimal set of parameters that minimize the estimation error. These values were then applied during the initialization step, as detailed in the pseudo-code of Algorithm 1.

To better understand the behavior of these discrepancies, we now proceed with a detailed analysis of the error distribution. The results presented in Figure 8a show that **32.4%** of the estimations are exact, meaning they are perfectly equal to the generated value. In contrast, **29.2%** of the cases correspond to an overestimation, with an average error of $+1.49$ photoelectrons, while **38.4%** of the cases correspond to an underestimation, with an average error of -1.82 photoelectrons.

A detailed analysis of the non-exact errors confirms a slight tendency of the system to underestimate the values. The most frequent error is -1 p.e., accounting for **19.8%** of the errors alone, followed by $+1$ photoelectron with **19.1%**. Larger errors (± 3 p.e. or more) remain much less frequent.

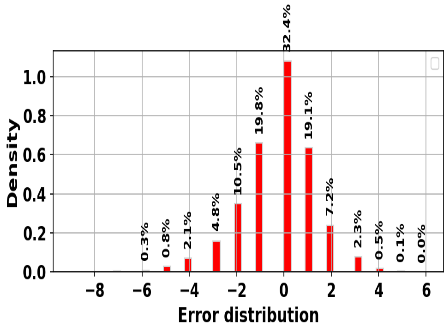

(a) The error distribution.

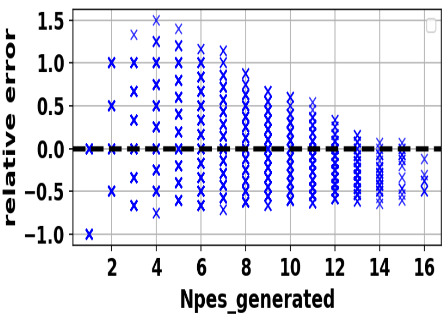

(b) The relative error distribution.

Figure 8: Error and relative error distributions.

Moreover, the relative error was computed to assess the precision of $N_{\text{pes}}^{\text{estimated}}$ by normalizing the previously calculated absolute error (as shown in Figure 8a) with respect to $N_{\text{pes}}^{\text{generated}}$, as defined in Equation 2.

$$\text{Relative Error} = \frac{N_{\text{pes}}^{\text{estimated}} - N_{\text{pes}}^{\text{generated}}}{N_{\text{pes}}^{\text{generated}}} \tag{2}$$

Figure 8b illustrates the variation of the relative error for each pair of $N_{\text{pes}}^{\text{generated}}$, The relative errors remain below the intrinsic contribution from statistical fluctuations in the number of photoelectrons, indicating that further technical optimizations would have little impact and validating the chosen estimation approach.

5.2 Single Line Multi-Time Over Threshold SL-MTOT

In the case of the SL-MTOT, the same analysis was applied, with the main difference lying in the integration strategy. Instead of a single threshold, our simulation used three thresholds $(\text{th}_1, \text{th}_2, \text{th}_3)$, resulting in three types of ToT integrations. These were implemented as follows:

$$E_{\text{rect}} = \text{th}_1\text{TOT}_1 + (\text{th}_2 - \text{th}_1)\text{TOT}_2 + (\text{th}_3 - \text{th}_2)\text{TOT}_3 \tag{3}$$

$$\begin{aligned} E_{\text{trap}} &= \frac{1}{2}(\text{th}_1 + \text{th}_2)\text{TOT}_1 + \frac{1}{2}(\text{th}_3 - \text{th}_1)\text{TOT}_2 \\ &\quad + \frac{1}{2}(\text{th}_3 - \text{th}_2)\text{TOT}_3 \end{aligned} \tag{4}$$

$$\begin{aligned} E_{\text{cross}} &= \frac{1}{2}(\text{th}_1 + \text{th}_2)\text{TOT}_1 + \frac{1}{2}(\text{th}_3 - \text{th}_1)\text{TOT}_2 \\ &\quad + \frac{1}{2}(\text{th}_3 - \text{th}_2)\frac{\text{TOT}_2\text{TOT}_3}{\text{TOT}_2 - \text{TOT}_3} \end{aligned} \tag{5}$$

By applying the $N_{\text{pes}}^{\text{generated}}$ across 50,000 simulated events, we analyzed the error distribution for each integration model. As summarized in the table 1, the error levels are generally higher than those observed with the SDM-1bit. Among the three methods, the crossing-point approach shows the best performance, with only **13.64%** of the events correctly estimated, while underestimation remains dominant.

Table 1: Integration methods with associated errors

Method / Estimation	**Rectangular**	**Crossing Point**	**Trapezoidal**
Correctly estimated	11.88%	13.64%	13.24%
Overestimated	25.26%	33.48%	27.56%
Underestimated	62.86%	52.88%	59.20%

Additionally, when analyzing the error distribution per p.e.s for the crossing-point method, a clear discrepancy emerges,as shown in Figure 9. The errors span nearly the entire dynamic range and follow a quasi-Gaussian distribution, with a standard deviation

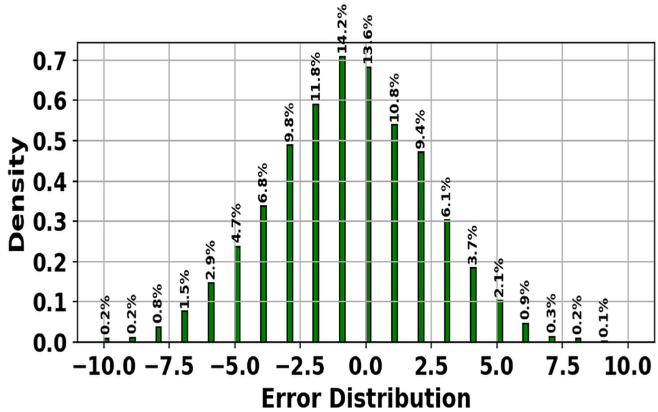

Figure 9: Error Distribution of the Crossing-Point Integration Method.

close to 3 p.e.s. This indicates that the estimation error extends across approximately 90% of the $N_{\text{pes}}^{\text{estimeted}}$ values. Moreover, errors confined within ±1 photoelectron account for less than **39%** of the total, highlighting a limited precision at the single-photoelectron level.

When analyzing the overall response across the 50,000 samples for each SL-MTOT integration method, the correlation between the $N_{\text{pes}}^{\text{estimeted}}$ and the ToT values is shown in the figure 10. A clear discrepancy is observed between the $N_{\text{pes}}^{\text{estimeted}}$ and the ideal fit line based on the $N_{\text{pes}}^{\text{generated}}$.

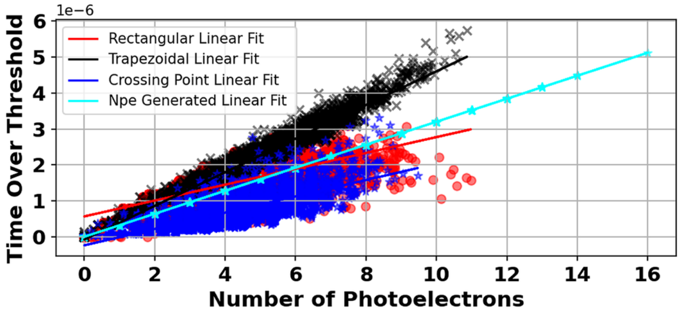

Figure 10: Correlation between the $\text{Npes}_{\text{generated}}$ and the $\text{Npes}_{\text{estimeted}}$ for the three integration methods.

This discrepancy arises from the distribution of timestamps at the XOR output. In previous works where this method was used to estimate gamma-ray energy[16], in 91% of the events, the recorded photons clouds had 6 edge crossings, and therefore 6 different timestamp values, corresponding to combinations from the three signals (TOT1, TOT2 and TOT3), as defined by the related equation (3), (4) et (5).

However, in our case, as shown in the figure 11, the timestamp count distribution is spread over various values, leading to a broader and less constrained error distribution

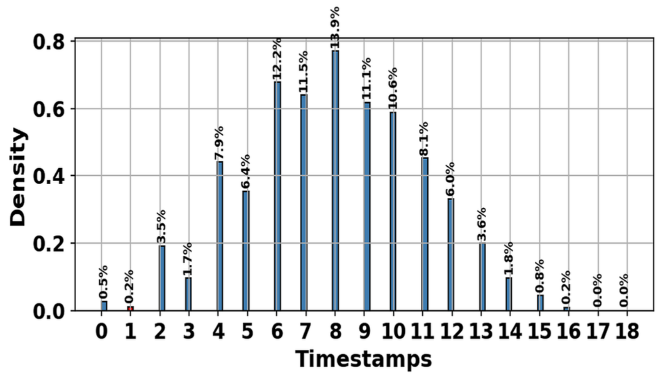

Figure 11: The XOR timestamps distribution.

across the dynamic range. This is further emphasized by the fact that, unlike in typical gamma-ray energy estimation, we are counting discrete N_{pes}, which introduces more granularity and sensitivity to timestamp count variation.

6 Discussion

The results show that the SDM-1Bit FEE accurately estimates $N_{pes}^{generated}$ within ±1 photoelectron in approximately **71.3%** of cases. This highlights both its single-photoelectron sensitivity and its ability to resolve individual p.e.s. Furthermore, by integrating machine learning techniques into the backend electronics, further improvements are expected in the conversion between N_{pes} and the time-over-threshold once data acquisition becomes possible, even in the presence of pile-up. In addition to its estimation capabilities, the SDM-1Bit also offers high flexibility for detector scaling, along with the advantages of low power consumption, low noise, and cost-effectiveness.

Unlike the SDM-1Bit, the SL-MTOT FEE is excluded for two main reasons. First, the error distribution of the SL-MTOT is broader and less confined within the dynamic range, with a standard deviation of 3 p.e.s, which can negatively affect sensitivity to single photoelectrons. As a consequence of the wider spread of the timestamp distribution, the SL-MTOT achieves an accurate estimation of the number of p.e.s within ±1 photoelectron in approximately **38.6%** of cases. Second, increasing the number of thresholds significantly raises the number of required comparators and digital readout channels, resulting in greater system complexity, particularly in terms of power consumption and the hardware resources needed for scaling.

A third configuration, dynamic time over threshold DTOT (shown in Figure 4), was also initially considered. However, it was excluded from simulation due to its reliance on a dynamic threshold generation circuit that closely mimics the input signal shape using an RC network and a monostable multivibrator. This approach is less suitable for XEMIS applications, where the objective is to count discrete photoelectrons following a Poisson distribution with pile-up. In this context, the dynamic threshold would also need to vary accordingly, which adds complexity. Moreover, the DTOT FEE presents a relatively high dead time, which limits its effectiveness in detecting closely spaced events.

Ultimately, the results point to a solution using the SDM-1Bit, combined with a cryogenic transimpedance amplifier based on SiGe HBT technology (LMH6629). It meets the XEMIS specifications and reliably enables single-photon detection using a 4×4 array of VUV-MPPCs (S13371-6050CQ-02)

7 Conclusion and outlook

In this paper, we presented the development strategy for a new cryogenic scintillation detection system for XEMIS3, intended to replace the current setup based on the PMT + XSRETOT FEE in the XEMIS project. The approach began with defining the system specifications for a 6×6mm² single-channel detection surface. A review of cryogenic considerations was then conducted to identify key design guidelines for ensuring the stable operation of commercial components at low temperatures. Based on these specifications, three FEE architectures were simulated and evaluated. The results demonstrated the effectiveness of the SDM-1bit design as a suitable candidate FEE, with single-photon sensitivity and **71.3%** ±1p.e detection efficiency, compared to the current XSRETOT system, which operates with a threshold level of up to 1p.e. This makes it a promising option to support future iterations of full-body imaging in the upcoming XEMIS3 phase.

The next phase will focus on designing a printed circuit board (PCB) integrating the proposed cryogenic scintillation detector system for a single 6×6mm² detection channel, with the objective of experimentally characterizing its response at liquid Xenon temperature (165K) and validating the results against simulation.

References

[1] Simon R. Cherry, James A. Sorenson, and Michael E. Phelps, *Physics in Nuclear Medicine*, Elsevier, 2012.

[2] P. Lecoq et al., "Roadmap toward the 10 ps time-of-flight PET challenge," Physics in Medicine & Biology, vol. 65, no. 21, p. 21RM01, Oct. 2020. DOI: 10.1088/1361-6560/ab9500

[3] F. Neumaier, B. D. Zlatopolskiy, and B. Neumaier, "Mutated Isocitrate Dehydrogenase (mIDH) as Target for PET Imaging in Gliomas," *Molecules*, vol. 28, no. 7, p. 2890, Mar. 2023.
DOI: 10.3390/molecules28072890

[4] M. Toussaint et al., "Improvement of Spatial Resolution with Iterative PET Reconstruction using UltraFast TOF," IEEE Transactions on Radiation and Plasma Medical Sciences, vol. 5, no. 5, pp. 729–737, 2021. DOI: 10.1109/TRPMS.2020.3033561

[5] C. Grignon et al., "Nuclear medical imaging using $\beta + \gamma$ coincidences from ^{44}Sc radio-nuclide with liquid xenon as detection medium," Nuclear Instruments and Methods in Physics Research Section A, vol. 571, no. 1, pp. 142–145, 2007. DOI: 10.1016/j.nima.2006.10.048

[6] G. Llosá and M. Rafecas, "Hybrid PET/Compton-camera imaging: an imager for the next generation," The European Physical Journal Plus, vol. 138, no. 3, p. 214, 2023. DOI: 10.1140/epjp/s13360-023-03805-9

[7] S. Katal et al., "Advantages and Applications of Total-Body PET Scanning," Diagnostics (Basel), vol. 12, no. 2, Feb. 2022.

[8] N. S. Iguiñiz et al., "The PETALO project," *Journal of Instrumentation*, vol. 19, no. 03, p. C03059, Mar. 2024.
DOI: 10.1088/1748-0221/19/03/C03059

[9] Y. Zhu, Development of the XEMIS2 liquid xenon Compton camera for 3-gamma imaging: studies and optimization of scintillation light measurements, Ph.D. dissertation, École nationale supérieure Mines-Télécom Atlantique, Jun. 2021.
Disponible en ligne : https://theses.hal.science/tel-03374269

[10] F. Shi, J. Lü, H. Lu, H. Y. Wang, Y.-Q. Ma, T. Hu, L. Zhou, M. Cai, L. J. Sun, B. X. Yu, J. Fang, Y. G. Xie, Z. H. An, Z. G. Wang, M. Gao, X. Li, Y. B. Xu, P. Wang, X. L. Sun, H. Wang, "Comparative studies of silicon photomultipliers and traditional vacuum photomultiplier tubes," *Chin. Phys. C*, vol. 35, p. 50, Jan. 2011. [Online]. Available: https://doi.org/10.1088/1674-1137/35/1/011

[11] S. Ogawa, "Liquid xenon calorimeter for MEG II experiment with VUV-sensitive MPPCs," Nuclear Instruments and Methods in Physics Research Section A, vol. 845, pp. 528–532, 2017.
DOI: 10.1016/j.nima.2016.06.085

[12] A. Hahn, R. Mirzoyan, A. Dettlaff, D. Fink, D. Mazin, and M. Teshima, "Direct comparison of SiPM and PMT sensor performances in a large-size imaging air Cherenkov telescope," *Nucl. Instrum. Methods Phys. Res., Sect. A*, vol. 1064, p. 169350, Jul. 2024. [Online]. Available: http://dx.doi.org/10.1016/j.nima.2024.169350

[13] J. Du and T. Jones, "Technical opportunities and challenges in developing total-body PET scanners for mice and rats," EJNMMI Physics, vol. 10, no. 1, p. 2, Jan. 2023.
DOI: 10.1186/s40658-022-00523-6

[14] H. Homulle and E. Charbon, "Performance characterization of Altera and Xilinx 28 nm FPGAs at cryogenic temperatures," in *Proc. 2017 Int. Conf. on Field Programmable Technology (ICFPT)*, pp. 25–31, 2017.
DOI: 10.1109/FPT.2017.8280117

[15] Z. Zhao et al., "A Novel Read-Out Electronics Design Based on 1-Bit Sigma-Delta Modulation," IEEE Transactions on Nuclear Science, vol. 64, no. 2, pp. 820–828, 2017.
DOI: 10.1109/TNS.2017.2648787

[16] H. Chu et al., "Single-line multi-voltage threshold method for scintillation detectors," Journal of Instrumentation, vol. 18, no. 06, p. P06021, Jun. 2023.
DOI: 10.1088/1748-0221/18/06/P06021

[17] K. Shimazoe et al., "Dynamic Time Over Threshold Method," IEEE Transactions on Nuclear Science, vol. 59, no. 6, pp. 3213–3217, 2012.
DOI: 10.1109/TNS.2012.2215338

[18] M. D'Incecco, C. Galbiati, G. K. Giovanetti, G. Korga, X. Li, A. Mandarano, A. Razeto, D. Sablone, and C. Savarese, "Development of a very low-noise cryogenic preamplifier for large-area SiPM devices," *IEEE Trans. Nucl. Sci.*, vol. 65, no. 4, pp. 1005–1011, Apr. 2018. [Online]. Available: http://dx.doi.org/10.1109/TNS.2018.2799325

[19] N. Gallice, A. Zani, P. Sala, M. Lazzaroni, M. Citterio, and A. Andreani, "Development of a design for SiPMs readout in cryogenic environment for large area photon detectors," in *Proc. 2021 IEEE Int. Instrum. Meas. Technol. Conf. (I2MTC)*, 2021, pp. 1–6. [Online]. Available: https://doi.org/10.1109/I2MTC50364.2021.9459995

[20] M. D'Incecco, C. Galbiati, G. K. Giovanetti, G. Korga, X. Li, A. Mandarano, A. Razeto, D. Sablone, and C. Savarese, "Development of a novel single-channel, 24 cm^2, SiPM-based, cryogenic photodetector," *IEEE Trans. Nucl. Sci.*, vol. 65, no. 1, pp. 591–596, Jan. 2018. [Online]. Available: http://dx.doi.org/10.1109/TNS.2017.2774779

[21] J. D. Cressler, "Operation of SiGe bipolar technology at cryogenic temperatures," *J. Phys. IV France*, vol. 4, Jun. 1994. [Online]. Available: http://dx.doi.org/10.1051/jp4:1994616

[22] N. Dinu, A. Nagai, and A. Para, "Studies of MPPC detectors down to cryogenic temperatures," *Nucl. Instrum. Methods Phys. Res., Sect. A*, vol. 787, pp. 275–279, 2015, New Developments in Photodetection NDIP14. [Online]. Available: https://www.sciencedirect.com/science/article/pii/S0168900214015174

[23] H. Otono, S. Yamashita, T. Yoshioka, H. Oide, T. Suehiro, and H. Hano, "Study of MPPC at liquid nitrogen temperature," presented at a conference or internal report, 2007. [Online]. Available: N/A

[24] J. M. Fernández-Tenllado, R. Ballabriga, M. Campbell, D. Gascón, S. Gómez, and J. Mauricio, "Optimal design of single-photon sensor front-end electronics for fast-timing applications," in *Proc. 2019 IEEE Nucl. Sci. Symp. Med. Imag. Conf. (NSS/MIC)*, 2019, pp. 1–5. [Online]. Available: https://doi.org/10.1109/NSS/MIC42101.2019.9059805

[25] L. Wang, M. Y. Guan, H. J. Qin, C. Guo, X. L. Sun, C. G. Yang, Q. Zhao, J. C. Liu, P. Zhang, Y. P. Zhang, W. X. Xiong, Y. T. Wei, Y. Y. Gan, and J. J. Li, "Characterization of VUV4 SiPM for liquid argon detector," *J. Instrum.*, vol. 16, no. 07, p. P07021, Jul. 2021. [Online]. Available: https://dx.doi.org/10.1088/1748-0221/16/07/P07021

[26] T. Pershing, J. Xu, E. Bernard, J. Kingston, E. Mizrachi, J. Brodsky, A. Razeto, P. Kachru, A. Bernstein, E. Pantic, and I. Jovanovic, "Performance of Hamamatsu VUV4 SiPMs for detecting liquid argon scintillation," *J. Instrum.*, vol. 17, no. 04, p. P04017, Apr. 2022. [Online]. Available: http://dx.doi.org/10.1088/1748-0221/17/04/P04017

[27] K. Ozaki, S. Kazama, M. Yamashita, Y. Itow, and S. Moriyama, "Characterization of new silicon photomultipliers with low dark noise at low temperature," *J. Instrum.*, vol. 16, no. 03, p. P03014, Mar. 2021. [Online]. Available: https://dx.doi.org/10.1088/1748-0221/16/03/P03014

[28] D. Marano *et al.*, "Silicon Photomultipliers Electrical Model Extensive Analytical Analysis,"
IEEE Transactions on Nuclear Science, vol. 61, no. 1, pp. 23–34, 2014.
DOI: 10.1109/TNS.2013.2283231

[29] S. E. Derenzo, W.-S. Choong, and W. W. Moses, "Fundamental limits of scintillation detector timing precision,"
Physics in Medicine & Biology, vol. 59, no. 13, p. 3261, 2014.
DOI: 10.1088/0031-9155/59/13/3261

[30] J. Nossent, P. Elsen, and W. Bauwens, "Sobol' sensitivity analysis of a complex environmental model," *Environmental Modelling & Software*, vol. 26, no. 12, pp. 1515–1525, 2011. DOI: 10.1016/j.envsoft.2011.08.010